Microstructures and deformation mechanisms in Opalinus Clay: insights from scaly clay from the Main Fault in the Mont Terri Rock Laboratory (CH)

Ben Laurich [1], Janos L. Urai [1], Christophe Nussbaum [2]

5   [1]Structural Geology, Tectonics and Geomechanics, RWTH Aachen University, Lochnerstr. 4-20, D-52056 Aachen, Germany
[2] Mont Terri Consortium Federal Office of Topography swisstopo, Route de la Gare 63, CH-2882 St-Ursanne, Switzerland

Correspondence to: Ben Laurich (b.laurich@ged.rwth-aachen.de)

Abstract. The Main Fault in the shaly facies of Opalinus Clay is a small reverse fault formed in slightly overconsolidated claystone at around one km depth. The fault zone is up to 6 m wide, with micron-thick shear zones, calcite and celestite

10   veins, scaly clay and clay gouge. Scaly clay occurs in up to 1.5 m wide lenses, providing hand specimens for this study. After mapping of the macroscopic fabric at 1 m - 0.1 mm scale, Broad Ion Beam polishing combined with scanning electron microscopy (BIB-SEM) was used to study microscale deformation mechanisms. Results show a network of thin shear zones and microveins, separating angular to lensoid microlithons between 10 cm and 10 µm in diameter, with slickensided surfaces. Samples can be easily disintegrated into individual microlithons because of the very low tensile strength of the thin

15   shear zones. Analyses of the size of microlithons show a power law distribution.

We present a model to explain the progressive formation of a self-similar network of anastomosing thin shear zones in a fault relay. The relay provides the boundary conditions for macroscopically continuous deformation. Localisation of strain in thin shear zones which are locally dilatant, and precipitation of calcite veins in dilatant shear fractures evolves into complex microscale re-partitioning of shear, forming new shear zones while the microlithons remain much less deformed internally

20   and the volume proportion of the µm-thick shear zones slowly increases. Grain scale deformation mechanisms are: microfracturing, boudinage and rotation of mica grains, pressure solution of carbonate fossils and pore collapse during ductile flow of the clay matrix. This study provides a microphysical basis to relate microstructures to macroscopic observations of strength and permeability of the Main Fault, and extrapolating fault properties in long term deformation.

1   Introduction

25   Scaly clay is an enigmatic soft rock with important differences in rheological and hydrological behaviour compared to its more competent protolith. There have been many studies of scaly clays, because of their geotechnical importance and role in detachment faulting. A rock comprises a scaly fabric if it splits along an anastomosing network of fractures into microlithons. Scaly clay is generally seen to have formed by deformation, and occurs in several fault settings (cf. Vannucchi et al., 2003), such as in drill cores from décollement zones of clay-rich accretionary prisms: Barbados (Labaume et al., 1997;

Maltman et al., 1997; Takizawa and Ogawa, 1999) and more recently Tohoku (Chester et al., 2013; Ujiie et al., 2013). Several other studies do not use the term scaly clay, however the rocks described contain complex shear zone arrays between microlithons - this is termed scaly clay by other authors (e.g. Arch and Maltman, 1990; Ismat, 2013; Maltman, 1987; Vitone et al., 2013; Vollmer and Bosworth, 1984).

5 Due to its fragile nature, intact scaly clay is difficult to sample and commonly weathered in surface outcrops. The Mont Terri Rock Laboratory in Switzerland offers a world class site with excellent sampling conditions of well-preserved scaly clay.

We studied scaly clay from the so-called Main Fault in the shaly facies of Opalinus Clay (OPA) at the Mont Terri Rock Laboratory (Figure 1). We observed five major fault structures: (1) slickensides on fractured surfaces, which are in cross-sectional view associated to (2) μm- thin shear zones of slickenside-parallel oriented particles, (3) clay gouge, (4) calcite and

10 celestite veins and (5) scaly clay aggregates. In a first publication, Laurich at al. (2014) focused on the evolution of veins and thin shear zones in the damage zone of the Main Fault, and showed strong particle reorientation and collapse of porosity due to deformation. The paper proposed that the scaly clay evolved by the progressive development of an anastomosing network of micro-shear zones. In this article, we present detailed observations on the scaly clay aggregates to document the geometry, size distribution and microstructure of microlithons, shear zones and microveins, on which we base a model for the evolution

15 of scaly clay in this setting.

The Main Fault is a 1 m to 6 m wide fault zone (Figure 2). It is interpreted as a reverse fault with about 10 m offset. Due to the fault-bend folding of the Mont Terri anticline, the Main Fault was passively steepened from 20° to 45°. It developed during the late Miocene (Nussbaum et al., 2011, accepted) at temperatures below 55 °C in a slightly over consolidated protolith, after burial to 1350 m in Late Cretaceous (Mazurek et al., 2006). Packer tests yielded hydraulic conductivities of

20 2 x 10^{-13} m/s for the protolith and 1 x 10^{-12} m/s to 1 x 10^{-13} m/s for the Main Fault (Bossart and Wermeille, 2003; Thury and Bossart, 1999). Profiles of several pore-water geochemical tracers are not perturbed across the Main Fault (Mazurek et al., 2011; Pearson et al., 2003; Rübel et al., 2002). This indicates diffusion as the main transport mechanism acting at least since the onset of influx from meteoric waters (Bossart and Wermeille, 2003): the Main Fault at present is of very low permeability and provides a well-documented example of a sealing fault in claystone.

25 **2   Methods**

We collected hand specimens from the outcrop walls in gallery 08 and 98 in the Mont Terri Rock Laboratory (Figure 1) as well as from six fault-penetrating drill cores (BPS12, BPS13, BPS14, BFS1, BFS2 and BFS3). Sampling and detailed field observations were based on field maps of the outcrop (Figure 2). Where possible, the sample orientation was marked and slickenside orientation noted.

30 On site, the scaly clay samples were treated in two ways: (1) stabilization in vacuum-sealed bags or by resin impregnation for transport or (2) gentle disintegration by hand into microlithons which were much harder and did not disintegrate, separating the product into large (cm- size) and small fractions by hand, photographing the result and packing in plastic bags.

After unpacking, all intact samples (1) were resin stabilized, diamond-cut dry parallel to slickensides (by visual observation these had a clear preferred orientation consistent with the fault's inferred movement direction) and perpendicular to the main foliation, and polished dry with carbide papers. One of the two polished halves was decorated by contact with water for a few seconds and quick drying in air. This technique caused a sight differential swelling of the polished surface, so that

5   foliations and shear zones became visible in reflected light, and could be photographed with a resolution of 0.05 mm to provide a basis for manual interpretation of bedding and shear zones.

In the disintegrated samples (2), microlithon size fractions of the samples were measured by gentle sieving (mesh sizes between 8 and 0.063 mm). Subsequently, morphology and microstructure of selected microlithons were analysed. Size distributions of microlithons in each sieve-fraction were measured by separating a small subsample of each sieve fraction,

10   dispersing the microlithons on a white paper sheet and digital image analysis (DIA) using the routines *analyse particles* and *minimum bounding geometry* of the software *Fiji* 1.5b and *ArcGIS* 10.2. Representativeness of the subsampling was tested by the cone and quartering technique (Brittain, 2002). The total number of microlithons per sieve-fraction was then estimated by multiplying with the weight ratio of the sieve fraction and the subsample. We carried this out for microlithon size fractions down to 0.25 mm in diameter.

15   For detailed microstructural study, we used microlithons from all size fractions and intact hand-specimens (those halves of the samples which were kept dry). These subsamples were broad-ion-beam (BIB) polished (*cf.* Desbois et al., 2009; Hemes et al., 2013; Houben et al., 2013; Klaver et al., 2012; Laurich et al., 2014) and subsequently imaged with a Zeiss supra 55 scanning electron microscope (SEM). The BIB polishing removed 100 µm of sample material to create 2 mm² flat surfaces (+/- 5 nm roughness as determined by Klaver et al. (2012)), free of mechanical polishing artefacts. We used a JEOL

20   SM09010 Ar-BIB cross-section polisher operating at 6 kV and 150 – 200 µA for 8 hours. Sample V12-1 was polished using a Tic3x Leica Ar-BIB operating for 1.5 h at 7 – 3 kV with up to 2.3 mA. Moreover, we used reflected light microscopy (RLM) using a Zeiss Axiovison microscope with magnifications up to 10x. For multi-scale analysis, we stitched RLM and SEM micrographs into large mosaics of up to 250 individual images using the software *Autopano* vers. 2.6.

All methods were applied with great care in handling and, except for the water immersion technique, always without the use

25   of water. Unloading / desiccation fractures did form along pre-existing shear zones, always showing slickenlines on the fracture walls if separated. Other artefacts were not observed.

Applying these methods (*cf.* Figure 3), we obtained the following data: (1) digitized vector networks of bedding foliation and shear zones, (2) microlithon size distributions of two disintegrated hand-specimens and (3) BIB-SEM and BIB-RLM images of the microstructure of intact scaly clay aggregates and disintegrated scaly clay microlithons.

30   We present first our results on microlithon size distributions and microlithon microstructure followed by a calculation of the vol.-% of strained material and by a detailed description of shear zone geometries in scaly clay.

3   Results

Scaly clay from the Mont Terri Rock Laboratory is present in the outcrop walls and in some drill cores of the Main Fault. Figure 4a shows an intact sample that is easily disintegrated into fragments (Figure 4b). These fragments can at first be further disintegrated by gentle hand manipulation. The residual microlithons are much harder to break. After disintegration, all microlithons reveal shiny slickensides (Figure 4b, Figure 5d and e), showing that the sample invariably disintegrated along pre-existing, non-cohesive shear zones. The largest sampled microlithons are about 7 cm long.

3.1   The size distribution of microlithons

The size distributions of scaly clay microlithons were determined in two samples: BPS12-SC1 (605.2 g) and BFS1-SC1 (508.1 g). They were retrieved from drill cores BPS12 and BFS1 (Figure 1). Figure 5a gives the measured sieve fraction weights for sample BPS12-SC1. The weighing was repeated after every 2 minutes of sieving. With increasing sieving time and with increasing vibration energy, the smaller fractions increased in weight as more large particles got divided into smaller microlithons (Figure 5a). As the weighing curves did not significantly change after 10 minutes of sieving, the vibration intensity was increased from 1.2 mm to 1.8 mm vibration amplitude. This stronger vibration enhanced the microlithon disintegration but may also have resulted in microlithon abrasion. Because the results of 4 minutes to 6 minutes of high vibration sieving differ only slightly, the sieving was stopped. We interpret this to show that this treatment largely disintegrated the aggregate into its microlithons, without creating too many small particles by abrasion. This is supported by RLM and SEM, which shows the vast majority of microlithons being bound by shear zones which fracture into polished slickensided surfaces (Figure 5c-f).

After this sieving procedure, subsamples of the sieved fractions were analysed with DIA: a log-log diagram in Figure 5b shows a histogram of microlithon frequencies vs. microlithon area for both samples: BPS12-SC1 and BFS1-SC1. The frequencies are noted with respect to bin width (which is exponentially increasing) and are normalized by the total sample mass to ensure inter-sample comparability (see supplemental data). Power-law regression shows exponents of -2.3 and -2 for BPS12-SC1 and BFS1-SC1, respectively. Values below 0.32 mm² were excluded in the calculation of the regression lines. We infer that below this size electrostatic effects interfere with the separation of smaller microlithons, but see from BIB-SEM analyses (see below) that the microlithons can be as small as a few grains (~50 µm height). The upper limit of the regression analysis is bound by the sample size of about 10 cm. It is likely that a few larger microlithons would be found if one disintegrated a much larger (e.g. 50 kg) sample (Figure 2 and Figure 13a).

3.2   The microstructure of microlithons

Surfaces of freshly separated microlithons of different sizes were imaged by SEM. All show slickensides which are indistinguishable from the surfaces of solitary slickensides described by Laurich et al. (2015). The surfaces show locally matt patches (Figure 5d), being more abundant on smaller microlithons. We interpret this as microscopic fragments formed

during the disintegration and sieving process, attached to the surfaces by electrostatic forces. In a few cases, in cross section, microlithons show a few thin internal shear zones of parallel aligned clay minerals (Figure 7). These zones indicate that not all microlithons are fully disintegrated.

Keeping the above arguments in mind, and considering the similar trend of power law microlithon size distribution in both samples and the shiny surfaces, which bound the vast majority of the microlithons, we interpret these results to be a reasonable representation of the size distribution of the microlithons in the scaly clay of the Main Fault.

The flakes settle into a preferred orientation when embedded in resin, with their longest axes sub-horizontal. A cross-section of resin-embedded microlithons was cut and examined by RLM (Figure 6c). The shape of the microlithons (X-Y section) derived from minimum bounding rectangle geometry (Figure 6d), showing an average height-to-length ratio of 0.43, +/- 0.16. In vertical viewing direction (microlithons dispersed on a sheet of paper, Figure 6a and b), a total of 206 microlithons show a width-to-length ratio of 0.71, +/- 0.12.

At high resolution SEM, all slickensides are smoothly polished, revealing platy, sub-µm clay particles aligned parallel to the surface and the characteristic nanoparticles described in Laurich et al. (2015) (Figure 5f, Figure 8c and Figure 9b). Thus, we infer the slickensided microlithon boundaries to be formed by fracturing of µm-thin shear zones during sampling, such as reported in Laurich et al. (2014). Microlithon-internal µm-thin shear zones are shown exemplarily in Figure 8d.

By BIB-SEM, we detect a microlithon-internal fabric that is similar to undeformed fabric of OPA outside scaly clay. For comparison, Figure 9b-c shows details of scaly clay microlithons and Figure 9a shows a detail of an undeformed subsample. We see similarities in grain size distribution, grain shape and in grain orientation. Note also the isolated, dark and unstrained organic matter (OM) in both samples. Additionally, the preserved pores in siderites (Figure 9c) are an indicator for unstrained fabric (Houben et al., 2013). Frequently, lobate SiO_2 grain boundaries and truncated fossils suggest pressure solution-precipitation, to a comparable degree in both, deformed and undeformed material (Figure 9). We therefore interpret these features to be diagenetic microstructures. Figure 7c shows an intact calcite fossil in a microlithon, supporting the interpretation of tectonically unstrained microlithons.

Despite this strong microstructural similarity, we also spotted some differences between protolith and microlithons. Locally, especially in the "tails" of the microlithons, there is evidence for microlithon-internal deformation. First, and most obvious, are thin shear zones that cut the microlithons (Figure 7 and Figure 8). As stated above, this indicates that the scaly clay block is not fully disintegrated along all the in-situ shear zones. Moreover, Figure 9c suggests a higher fabric intensity compared to the undeformed sample and we interpret this as caused by less localized deformation of microlithons. Further signs for microlithon internal deformation are overgrowth structures and an increased density of larger calcite patches and veins as shown in Figure 7b and d. These patches and veins indicate pressure solution precipitation, complemented by percolation of additional fluids in order to provide the necessary calcium (Clauer et al., accepted). Moreover, we locally find particle bending and elongated OM particles in the vicinity of thin shear zones (Figure 7 - Figure 9). The calcite patches occur in geometric relation to microlithon internal shear zones. However, microlithon-internal deformation alters the protolithic fabric only to a limited extent and is found to be localized in isolated zones, leaving large microlithon volumes unaffected.

3.3 The vol.-% of strained material in scaly clay

With decreasing microlithon size, the vol-% of bounding shear zones per microlithon increases. The smallest microlithons consist for a large part of sheared clay. In contrast, the largest microlithons contain less than 1 vol.-‰ strained material. Thus, the power law exponent of the microlithon size distribution controls the calculation of strained material, i.e. for a small negative exponent, in particular down to around -2, small microlithons contribute less to the total sample volume than large ones and hence the strained volume is correspondingly low. In a rough estimation, the shear zones encasing the microlithons down to 41 µm height make up 0.19 vol.- % for sample BFS1-SC1 (exponent = -2.0) and 1.3 vol.-% for sample BPS12-SC1 (exponent = -2.3) (see supplemental data). For this estimation we considered a scale-independent average microlithon shape of two spherical caps facing each other. This is a strong simplification to estimate that the strained volume in scaly clay is as low as about 1 %. We suggest further studies on microlithon shapes.

4 Discussion

4.1 Fabric

Scaly clay is a prominent and easily recognizable part of the Main Fault. It occurs in elongated bodies of fault rock and is composed of lens-shaped, biconvex, elongated, variably sized microlithons (or phacoids, cf. Bosworth and Vollmer, 1981; Housen et al., 1996) that are separated by anastomosing thin shear zones and microveins. The microlithons are the building blocks of scaly clay: they are essentially undeformed and quite resistant to further disintegration. Microlithons of all sizes are roughly similar in shape, mostly with their longest axis parallel to the movement direction of the Main Fault (Figure 11). The slickensides on the microlithons also have this trend (dip-slip), scattered by the anastomosing geometry of the shear zones. The microlithon- bounding thin shear zones are 5 µm – 10 µm wide and identical in microstructure to those reported by Laurich et al. (2014) from the non-scaly parts of the Main Fault in OPA. We are currently investigating if the evolution of nm-sized clay particles in the slickensided surfaces (Figure 5f) may involve a combined process of cataclasis and authigenic precipitation from fluids as suggested by Clauer et al. (accepted). Moreover, we showed intact and reworked microveins within scaly clay, always bound to shear zones and often in the vicinity to gouge (Figure 7b, Figure 14). This indicates early to syn-tectonic vein precipitation. Neither the veins nor the thin shear zones show consistent overprintings and the microfolds are not refolded, suggesting a progressive development of the scaly clay during shearing in the Main Fault.

4.1.1 Comparison to other scaly clays

Our findings are comparable but also different to other scaly clays worldwide: According to the terminology of Vannucchi et al. (2003), the scaly fabric of Opalinus Clay from the Main Fault is defined by partings along localized zones of aligned grains in a matrix of poorly to slightly aligned clay minerals. We identified these localized zones as µm-thin shear zones similar to other scaly clays (e.g. Maltman, 1987) and classify scaly Opalinus Clay as comparable to scaly clay from the

6

Apennine detachment faults (Coli and Sani, 1990; Vannucchi and Maltman, 2000). Nevertheless, we see similarities (localized particle alignment, anastomosing shear zones, comparable microlithon shapes) also to scaly clays with a higher degree in fabric intensity such as those from tectonic mélanges and submarine accretionary prisms (Agar et al., 1989; Bettelli and Vannucchi, 2003; Chester et al., 2013; Labaume et al., 1997). Similar to all studies on the scaly clays mentioned above,

5 we interpret that finely distributed shearing is the main fabric generating process, with the occasional occurrence of S-C geometries at various scales.

4.1.2   Microlithon- internal deformation

It is a long-standing debate if microlithon internal fabric "shows any alignment of phyllosilicates", especially in scaly clay of accretionary prisms (Agar et al., 1989; Labaume et al., 1997; Prior and Behrmann, 1990; Vannucchi et al., 2003; Wallace et

10 al., 2003). Takizawa et al. (1999) and Housen et al. (1996) ask why bulk rock physical properties of scaly clay from the Barbados prism indicate a low degree of preferred particle orientation in depths where deformation appears to be most highly concentrated. A low degree of particle alignment is also found by Morgan and Kraig (1995) for the decollement zone of the Nankai accretionary prism. In contrast, microstructural SEM studies on Barbados scaly clay show strong preferred particle orientations (Cowan et al., 1984; Labaume et al., 1997; Maltman et al., 1997; Moore et al., 1986; Taylor et al., 1990). Our

15 observations have shown that deformation is strongly partitioned into µm-thin shear zones of aligned particles, whilst the microlithons remains largely undeformed: We observed in the microlithons intact fossils, similar grain sizes, grain shapes and a similar degree in grain alignment to undeformed fabric from non-scaly Opalinus Clay (Figure 9).

The network of the shear zones between the microlithons can be a spaced cleavage as shown in Figure 4a, anastomosing with variable density (Figure 10) to S-C foliations (Figure 13) with microfolds (right and left part in Figure 11). We also note

20 that in the lens-shaped scaly clay in Figure 13 the bedding has been rotated to vertical while in the surrounding undeformed rock the bedding is sub-horizontal, resulting in a kink-like geometry with strong development of scaly clay.

4.1.3   Different 'scaliness'

In agreement with the above observations, there are different intensities of scaly clay, i.e. scaly aggregates with different densities of thin shear zones and with different microlithon sizes (Figure 10). However, the volume of shear zones in scaly

25 clay is minor (< 1 vol.-%), even for aggregates with a high scaliness (see above). These findings are in concert with Housen et al. (1996) who proposed that most strain in the décollement of the Barbados prism has been accumulated by the volumetrically minor component of shear zones.

We note that the scales of observation used in this study do not yet allow full multiscale mapping of shear zones: It is not yet possible to map all shear zones with sub-micron resolution in the hand specimens which we mapped using optical

30 microscopy.

7

4.2 Mechanisms in the evolution of scaly clay

Even though scaly clays have been extensively studied, a comprehensive mechanical understanding of their evolution is missing. 'Scaly clay' is a descriptive term without any genetic connotation and there are many different mechanisms that can produce scaly fabric (cf. Vannucchi et al., 2003). In what follows we discuss and compare possible mechanisms for the
5   evolution of the scaly clay as part of the fault processes in the Main Fault.

4.2.1 Evolution of the initial segments of the Main Fault

As a response to tectonic stress, we infer that a series of shallow- dipping, incipient, curved thin shear zones formed the first localization of deformation in the phyllosilicate-rich, slightly overconsolidated OPA. We interpret this to be associated with intense softening in the thin shear zones (Ikari et al., 2011; Ingram and Urai, 1999; Kirkpatrick et al., 2015), caused by
10   collapse of porosity, breakup of cement, alignment of particles and the formation of nanoparticles and perhaps the associated temporary local increase in pore pressure. This localized deformation is interpreted to have interacted with slip along the bedding foliation (Haines et al., 2013; Ikari et al., 2011). In these shear zones it is much easier to keep sliding than to deform the protolith, but the geometry of the shear zones rapidly leads to 'locking-up' and associated stress concentrations, which initiate new shear zones. We propose that these initial shear zone networks develop into fault segments which coalesce
15   during further fault movement. It is the strike and dip relays between these segments (Nicol et al., 2002) that create the boundary conditions for macroscopically continuous deformation by sequentially developing, conjugate shear zones finally forming the scaly clay (cf. Figure 2 and Figure 13). The proposed evolution is sketched in Figure 15 and further discussed below.

Some insight in the mechanics of this process may be provided by the results of van der Zee (2001) who found an increased
20   differential stress in the restraining bends that causes a preferred deformation of the relays' interior. The deformation in the relay results in folding of the bedding to a steep orientation aided by slip along bedding, and is accompanied by conjugate shears (stage 2 in Figure 15): one as bedding parallel offset and the other as bedding perpendicular offset (cf. Carreras et al., 2010; McGrath and Davison, 1995; Nicol et al., 2002; Vollmer and Bosworth, 1984). This way, rhombohedral microlithons (Figure 4a), similar to the fabric of pencil cleavage (cf. Reks and Gray, 1982) form. However, Figure 6c shows more
25   elliptically shaped microlithons and Figure 15b and Figure 12 picture more curved shear zones that have been reported for other scaly clays, too. We interpret these to show that the shear zones formed progressively, with younger shear zone paths being influenced by the reactivation of older shears (stage 3 in Figure 15). The boundary conditions for this macroscopically continuous deformation are given by the relay between the initial segments (Figure 11, Figure 12, Figure 14). The interaction of the two sets of shears is illustrated in Figure 16, showing how progressively smaller microlithons are formed to
30   accommodate deformation around large microlithons. This model is also supported in Figure 8c, where a curved shear zone splays up next to a through-going shear zone, suggesting a relative age relation of the shears.

8

The process of progressive slicing up of fragments has been modelled by Sammis and King (2007), who showed the process of collisions of particles in a fault zone which fail by Mode I fracturing. With increasing displacement, they found a power law particle size distribution with increasing exponents. In the scaly clay of OPA, the fragments fail by shear, and the fragments are increasingly surrounded by the soft material of the shear zones which helps the microlithons flow past each other (Figure 16). This may lead to different power law exponents, which in this case also be used as an indicator of the degree of deformation.

In addition to the geometrical locking and fragmentation in a relay as described above, another mechanism is important: The evolution of pore pressure and effective stress. There are two relevant observations for this: The isolated calcite microveins and the network of shear zones with porosity collapse.

4.2.2   Dependency of strain and pore pressure changes

We infer that the shear zones in our samples were closed in situ (e.g. Figure 8d): the fracture with slickensides is interpreted to have resulted from excavation damage and sample handling (cf. Prior and Behrmann, 1990). This is supported by the extremely low permeability of the Main Fault shown by measurements in boreholes (Bossart and Wermeille, 2003; Thury and Bossart, 1999). Measurements in deformed Tohoku décollement samples (scaly clay), show a drastic permeability decrease perpendicular to shear direction (Ikari et al., 2013). Arch and Maltman (1990) found in laboratory experiments a higher permeability parallel to shear and Casciello et al. (2004) propose a mechanism of 'self-lubrication' of the shear zones. An interesting problem of scaly clay evolution is thus, that during the formation of a shear zone forming inside a microlithon, the pore collapse may create a temporary, local increase in pore pressure in the microlithons bound by the closed-cell network of shear zones with very low permeability. If the rate of pore pressure generation is faster than the permeability allows the pore pressure to dissipate, overpressure is generated (Vannucchi et al., 2003). On the other hand, the slight overconsolidation of OPA allowed dilation along some of the shear zones between the microlithons, which can cause rapid local redistribution of fluid and crystallization of the microveins. This, in turn, leads to local, temporary drop in fluid pressure that may promote locking of the shear zones and vein precipitation (cf. veins in Figure 7b and in Figure 14). Moore and Iverson (2002) found stable but episodic slip in ring shear tests of compacted, water saturated granular materials where pore pressure build-up leads to material weakening and shear-induced dilation leads to a decline of fluid pressure with consequent material strengthening. It would be interesting to try to quantify the local heterogeneities in pore pressure in the evolving Main Fault. A starting point for this could be the work of Cuss et al. (2012) reporting heterogeneous pore pressure distributions in clay-rich materials and the work of Amann and Vogelhuber (2015) who have reviewed the geomechanical studies of Opalinus Clay , discussing the many pitfalls of accurately measuring pore pressure during experiments. Although the pore pressure coefficients reported by Amann and Vogelhuber (2015) may allow estimating the local pore pressure increase in the microlithons surrounded by pore-collapsing shear zones, there is no information available on the permeabilities of OPA shear zones. In agreement to our considerations, experiments on Opalinus Clay by Cuss et al. (2011)

showed that conductivity decreases at low shear strain and increases at high shear strain due to the development of a complex shear network.

4.2.3 Evolution of scaly clay

In the sections above, we discussed how the macroscopically continuous deformation in the scaly clay of the Main Fault in OPA can result from deformation in relays between fault segments. Considering that the same evolutionary mechanism applies for all scaly clay aggregates in the Main Fault, we hypothesise a similar power law microlithon size distribution, may the aggregates show strong or little 'scaliness'.

Depending on the activity and propagation of the segments, scaly fabric in the relays may be preserved or further evolve by ongoing distributed shear. This can lead to a fully reworked protolith that eventually became gouge. The development of this gouge (Figure 14) is further discussed in a follow-up paper.

5 Conclusion

Scaly clay aggregates consist of elongated lens-shaped microlithons surrounded by µm-thin shear zones. The density of these shears is variable, leading to different scaliness. The shear zones surround microlithons of various sizes which are internally undeformed to slightly deformed (e.g. by bedding parallel shear in flexural slip of microfolds, development of cleavage). The size distribution of the recorded microlithons follows a power law; the upper and lower limit of which are not determinable from the data alone. However, we consider the smallest microlithon to be in the range of only a few grains wide and the largest in the order of 10 cm length, based on outcrop observations. The determined power-law exponent allows estimating the total deformed volume in the scaly clay, which is of the order of 1 vol.-%.

These findings are comparable to other scaly clays worldwide, but in particular remarkable is that an intense scaliness occurs with such a small offset (10 m).

We hypothesize that the power-law exponent depends on the evolutionary mechanism, not on the 'scaliness' of the scaly clay. Hence, aggregates from other localities (with differing mechanisms) might show variant exponents and this fabric property could thus be used to classify scaly clays.

Scaly clay from the Main Fault is highly deformed Opalinus Clay, formed by the progressive interaction of thin shear zones to generate new ones, evolving into a network of anastomosing shear zones between microlithons. We deduce that scaly clay formed by finely distributed brittle shear, caused by the boundary conditions of a fault relay deforming between segments of the evolving Main Fault. The extreme partitioning of strain is related to the very intense softening in the already anisotropic OPA, caused by collapse of porosity, breakup of cement, alignment of particles and the formation of nanoparticles and the possible associated local increase in pore pressure.

Our microstructural observations are in good agreement with the extremely low permeability of the Main Fault at present.

Extrapolation of laboratory deformation experiments to predict the long-term mechanical properties of faults in OPA requires incorporation of the different deformation mechanisms between laboratory and natural deformation.

6   Acknowledgements

7   References

Agar, S.M., Prior, D.J., Behrmann, J.H., 1989. Back-scattered electron imagery of the tectonic fabrics of some fine-grained sediments: Implications for fabric nomenclature and deformation processes. Geology 17, 901–904. doi:10.1130/0091-7613(1989)017<0901

Amann, F., Vogelhuber, M., 2015. Expert Report - Assessment of Geomechanical Properties of Intact Opalinus Clay.

Arch, J., Maltman, A., 1990. Anisotropic permeability and tortuosity in deformed wet sediments. J. Geophys. Res. Earth Planets 95, 9035–9045. doi:10.1029/JB095iB06p09035

Bettelli, G., Vannucchi, P., 2003. Structural stlyle of the offscraped Ligurian oceanic sequences of the Northern Apennines: New hypothesis concening the development concerning the development of me??lange block-in-matrix fabric. J. Struct. Geol. 25, 371–388. doi:10.1016/S0191-8141(02)00026-3

Bossart, P., Wermeille, S., 2003. Paleohydrological Study on the Surroundings of the Mont Terri Rock Laboratory, in: Heitzmann, P., Tripet, J.-P. (Eds.), Mont Terri Project – Geology, Paleohydrology and Stress Field of the Mont Terri Region, Geology Series. Federal Office for Water and Geology, Bern-Ittigen, pp. 45–64.

Bosworth, W., Vollmer, F.W., 1981. Bozworth_and_Vollmer_1981_JGeol.pdf. J. Geol. 551–568.

Brittain, H.G., 2002. Particle-Size Distribution II : Powdered Solids of sampling powdered solids. Pharm. Phys. 2, 1–5.

Carreras, J., Czeck, D.M., Druguet, E., Hudleston, P.J., 2010. Structure and development of an anastomosing network of ductile shear zones. J. Struct. Geol. 32, 656–666. doi:10.1016/j.jsg.2010.03.013

Casciello, E., Cesarano, M., Cosgrove, J.W., 2004. Shear deformation of pelitic rocks in a large-scale natural fault. Geol. Soc. London, Spec. Publ. 224, 113–125. doi:10.1144/GSL.SP.2004.224.01.08

Chester, F.M., Rowe, C., Ujiie, K., Kirkpatrick, J., Regalla, C., Remitti, F., Moore, J.C., Toy, V., Wolfson-Schwehr, M., Bose, S., Kameda, J., Mori, J.J., Brodsky, E.E., Eguchi, N., Toczko, S., 2013. Structure and composition of the plate-boundary slip zone for the 2011 Tohoku-Oki earthquake. Science (80-.). 342, 1208–1211. doi:10.1126/science.1243719

Clauer, N., Techer, I., Nussbaum, C., Laurich, B., accepted. Geochemical signatures of paleofluids in calcite from microstructures and matrix of the Main Fault in the Opalinus Clay: A contribution to the regional evolutionary model. Swiss J. Geosci.

Coli, M., Sani, F., 1990. Vein distribution in a thrust zone; a case history from the Northern Apennines, Italy Deformation mechanisms, rheology and tectonics. Geol. Soc. Spec. Publ. 54, 475–482. doi:10.1144/GSL.SP.1990.054.01.43

Cowan, D., Moore, J., Roeske, S.M., Lundberg, N., Lucas, S.E., 1984. Structural features at the deformation front of the Barbados Ridge Complex, Deep Sea Drilling Project LEG 78A. Initial Reports Deep Sea Drill. Proj. 78 535–548. doi:10.2973/dsdp.proc.78a.127.1984

Cuss, R.J., Harrington, J.F., Graham, C.C., Sathar, S., Milodowski, A.E., 2012. Observations of heterogeneous pore pressure distributions in clay-rich materials. Mineral. Mag. 76, 3115–3129. doi:10.1180/minmag.2012.076.8.26

Cuss, R.J., Milodowski, A., Harrington, J.F., 2011. Fracture transmissivity as a function of normal and shear stress: First results in Opalinus Clay. Phys. Chem. Earth 36, 1960–1971. doi:10.1016/j.pce.2011.07.080

Desbois, G., Urai, J.L., Kukla, P.A., 2009. Morphology of the pore space in claystones – evidence from BIB/FIB ion beam sectioning and cryo-SEM observations. eEarth Discuss. 4, 1–19. doi:10.5194/eed-4-1-2009

Haines, S.H., Kaproth, B., Marone, C., Saffer, D., Van der Pluijm, B., 2013. Shear zones in clay-rich fault gouge: A laboratory study of fabric development and evolution. J. Struct. Geol. 51, 206–225. doi:10.1016/j.jsg.2013.01.002

Hemes, S., Desbois, G., Urai, J.L., Craen, M. De, Honty, M., 2013. Variations in the morphology of porosity in the Boom Clay Formation: insights from 2D high resolution BIB-SEM imaging and Mercury injection Porosimetry. Netherlands J. Geosci. / Geol. en Mijnb. 92, 275–300.

Houben, M.E., Desbois, G., Urai, J.L., 2013. Pore morphology and distribution in the Shaly facies of Opalinus Clay (Mont Terri, Switzerland): Insights from representative 2D BIB–SEM investigations on mm to nm scale. Appl. Clay Sci. 71, 82–97. doi:10.1016/j.clay.2012.11.006

Housen, B.A., Tobin, H.J., Labaume, P., Leitch, E.C., Maltman, A.J., Party, O.D.P.L. 156 S.S., 1996. Strain decoupling across the decollement of the Barbados accretionary prism. Geology 24, 127–130.

Ikari, M., Kameda, J., Kopf, A., 2013. Frictional behavior of the plate boundary décollement zone in the Japan Trench, sampled during the Japan Trench Fast Drilling Project (JFAST): Implications for shallow coseismic slip propagation, in: EGU General Assembly Conference Abstracts.

Ikari, M.J., Marone, C., Saffer, D.M., 2011. On the relation between fault strength and frictional stability. Geology 39, 83–86. doi:10.1130/G31416.1

Ingram, G.M., Urai, J.L., 1999. Top-seal leakage through faults and fractures: the role of mudrock properties. Geol. Soc. London, Spec. Publ. 158, 125–135. doi:10.1144/GSL.SP.1999.158.01.10

Ismat, Z., 2013. Block-supported cataclastic flow within the upper crust. J. Struct. Geol. 56, 118–128. doi:10.1016/j.jsg.2013.08.010

Kirkpatrick, J.D., Rowe, C.D., Ujiie, K., Moore, J.C., Regalla, C., Remitti, F., Toy, V., Wolfson-Schwehr, M., Kameda, J.,

Bose, S., Chester, F.M., 2015. Structure and lithology of the Japan Trench subduction plate boundary fault. Tectonics 34, 53–69. doi:10.1002/2014TC003695

Klaver, J., Desbois, G., Urai, J.L., Littke, R., 2012. BIB-SEM study of the pore space morphology in early mature Posidonia Shale from the Hils area, Germany. Int. J. Coal Geol. 103, 12–25. doi:10.1016/j.coal.2012.06.012

5   Labaume, P., Maltman, A.J., Bolton, A., Tessier, D., Ogawa, Y., Takizawas, S., 1997. Scaly fabrics in sheard clays from the decollement zone of the Barbados accretionary prism, in: Shipley, T.R., Ogawa, Y., Blum, P., Bahr, J.M. (Eds.), Proceedings of the Ocean Drilling Program. pp. 59–77.

Laurich, B., 2015. Evolution of microstructure and porosity in faulted Opalinus Clay. RWTH-Aachen University.

Laurich, B., Urai, J.L., Desbois, G., Vollmer, C., Nussbaum, C., 2014. Microstructural evolution of an incipient fault zone in
10   Opalinus Clay: Insights from an optical and electron microscopic study of ion-beam polished samples from the Main Fault in the Mt-Terri underground research laboratory. J. Struct. Geol. 67, 107–128. doi:10.1016/j.jsg.2014.07.014

Maltman, A., Labaume, P., Housen, B., 1997. Structural geology of the décollement at the toe of the Barbados accretionary prism. Proc. Ocean Drill. Program, Sci. Results 156, 279–292.

Maltman, A.J., 1987. Shear zones in argillaceous sediments--an experimental study. Geol. Soc. London, Spec. Publ. 29, 77–
15   87. doi:10.1144/GSL.SP.1987.029.01.08

Mazurek, M., Alt-Epping, P., Bath, A., Gimmi, T., Waber, H.N., Buschaert, S., Cannière, P. De, Craen, M. De, Gautschi, A., Savoye, S., Vinsot, A., Wemaere, I., Wouters, L., 2011. Natural tracer profiles across argillaceous formations. Appl. Geochemistry 26, 1035–1064. doi:10.1016/j.apgeochem.2011.03.124

Mazurek, M., Hurford, A.J., Leu, W., 2006. Unravelling the multi-stage burial history of the Swiss Molasse Basin:
20   integration of apatite fission track, vitrinite reflectance and biomarker isomerisation analysis. Basin Res. 18, 27–50. doi:10.1111/j.1365-2117.2006.00286.x

McGrath, A.G., Davison, I., 1995. Damage zone geometry around fault tips. J. Struct. Geol. 17, 1011–1024. doi:10.1016/0191-8141(94)00116-H

Moore, J.C., Roeske, S., Cowan, D.S., Lundberg, N., Gonzales, E., Schoonmaker, J., Lucas, S.E., 1986. Scaly fabrics from
25   Deep Sea Drilling Project cores from forearcs. Geol. Soc. Am. Mem. 166, 55–74. doi:10.1130/MEM166-p55

Moore, P.L., Iverson, N.R., 2002. Slow episodic shear of granular materials regulated by dilatant strengthening. Geology 30, 843. doi:10.1130/0091-7613(2002)030<0843:SESOGM>2.0.CO;2

Morgan, J.K., Karig, D.E., 1995. Décollement processes at the Nankai accretionary margin, southeast Japan: Propagation, deformation, and dewatering. J. Geophys. Res. 100, 15221. doi:10.1029/95JB00675

30   Nicol, A., Gillespie, P.A., Childs, C., Walsh, J.J., 2002. Relay zones between mesoscopic thrust faults in layered sedimentary sequences. J. Struct. Geol. 24, 709–727. doi:10.1016/S0191-8141(01)00113-4

Nussbaum, C., Bossart, P., Amann, F., Aubourg, C., 2011. Analysis of tectonic structures and excavation induced fractures in the Opalinus Clay, Mont Terri underground rock laboratory (Switzerland). Swiss J. Geosci. 104, 187–210. doi:10.1007/s00015-011-0070-4

Nussbaum, C., Kloppenburg, A., Caer, T., Bossart, P., accepted. Tectonic evolution of the Mont Terri region, northwestern Swiss Jura: constraints from kinematic forward modelling. Swiss J. Geosci.

Pearson, F.J., Arcos, D., Bath, A., Boisson, J., Fernandez, A.M., Gäbler, H., Gaucher, E., Gautschi, A., Griffault, L., 2003. Mont Terri Project: Geochemistry of Water in the Opalinus Clay Formation at the Mont Terri Rock Laboratory, 5th ed. Federal Office for Water and Geology, Bern-Ittigen.

Prior, D.J., Behrmann, J.H., 1990. Thrust-related mudstone fabrics from the Barbados Forearc: A backscattered scanning electron microscope study. J. Geophys. Res. 95, 9055. doi:10.1029/JB095iB06p09055

Reks, I.J., Gray, D.R., 1982. Pencil structure and strain in weakly deformed mudstone and siltstone. J. Struct. Geol. 4, 161–176. doi:10.1016/0191-8141(82)90025-6

Rübel, A.P., Sonntag, C., Lippmann, J., Pearson, F.J., Gautschi, A., 2002. Solute transport in formations of very low permeability: Profiles of stable isotope and dissolved noble gas contents of pore water in the Opalinus Clay, Mont Terri, Switzerland. Geochim. Cosmochim. Acta 66, 1311–1321. doi:10.1016/S0016-7037(01)00859-6

Sammis, C.G., King, G.C.P., 2007. Mechanical origin of power law scaling in fault zone rock. Geophys. Res. Lett. 34, 2–5. doi:10.1029/2006GL028548

Takizawa, S., Ogawa, Y., 1999. Dilatant clayey microstructure in the Barbados décollement zone. J. Struct. Geol. 21, 117–122.

Taylor, E., Burkett, P.J., Wackier, J.D., Leonard, J.N., 1990. Physical Properties and Microstructural Response of Sediments to Accretion-Subduction: Barbados Forearc, in: Bennett, R.H., Bryant, W.R., Hulbert, M.H. (Eds.), Microstructure of Fine-Grained Sediments. Springer-Verlag, New York, pp. 213–228.

Thury, M., Bossart, P., 1999. The Mont Terri rock laboratory, a new international research project in a Mesozoic shale formation, in Switzerland. Eng. Geol. 52, 347–359. doi:10.1016/S0013-7952(99)00015-0

Ujiie, K., Tanaka, H., Saito, T., Tsutsumi, A., Mori, J.J., Kameda, J., Brodsky, E.E., Chester, F.M., Eguchi, N., Toczko, S., 2013. Low coseismic shear stress on the Tohoku-Oki megathrust determined from laboratory experiments. Science 342, 1211–4. doi:10.1126/science.1243485

van der Zee, W., 2001. Dynamics of fault gouge development in layered sand-clay sequences. RWTH Aachen.

Vannucchi, P., Maltman, A., Bettelli, G., Clennell, B., 2003. On the nature of scaly fabric and scaly clay. J. Struct. Geol. 25, 673–688. doi:10.1016/S0191-8141(02)00066-4

Vannucchi, P., Maltman, a. J., 2000. Insights into shallow-level processes of mountain building from the Northern Apennines, Italy. J. Geol. Soc. London. 157, 105–120. doi:10.1144/jgs.157.1.105

Vitone, C., Viggiani, G., Cotecchia, F., Hall, S. a., 2013. Localized deformation in intensely fissured clays studied by 2D digital image correlation. Acta Geotech. 8, 247–263. doi:10.1007/s11440-013-0208-9

Vollmer, F.W., Bosworth, W., 1984. Formation of melange in a foreland basin overthrust setting; example from the Taconic Orogen. Melanges; their nature, Orig. significance. doi:10.1130/SPE198-p53

Wallace, G., Moore, J.C., Dileonardo, C.G., 2003. Controls on localization and densi cation of a modern de ´ collement:
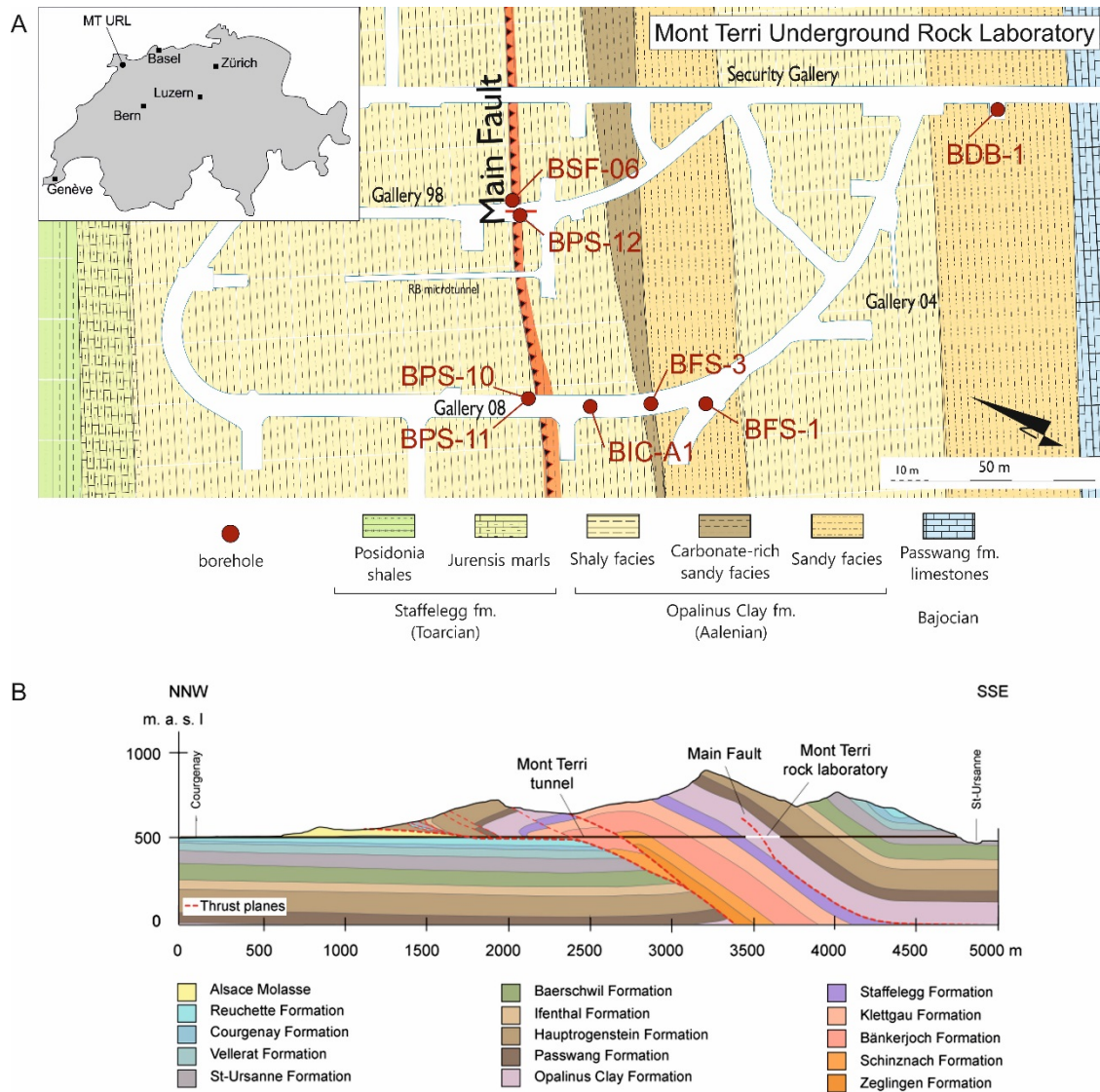
Figure 1: Geology of the Mont Terri Rock Laboratory (CH). A) Outline and facies map (plan-view), borehole locations indicated. B) 2D balanced cross-section after Nussbaum et al. (accepted).
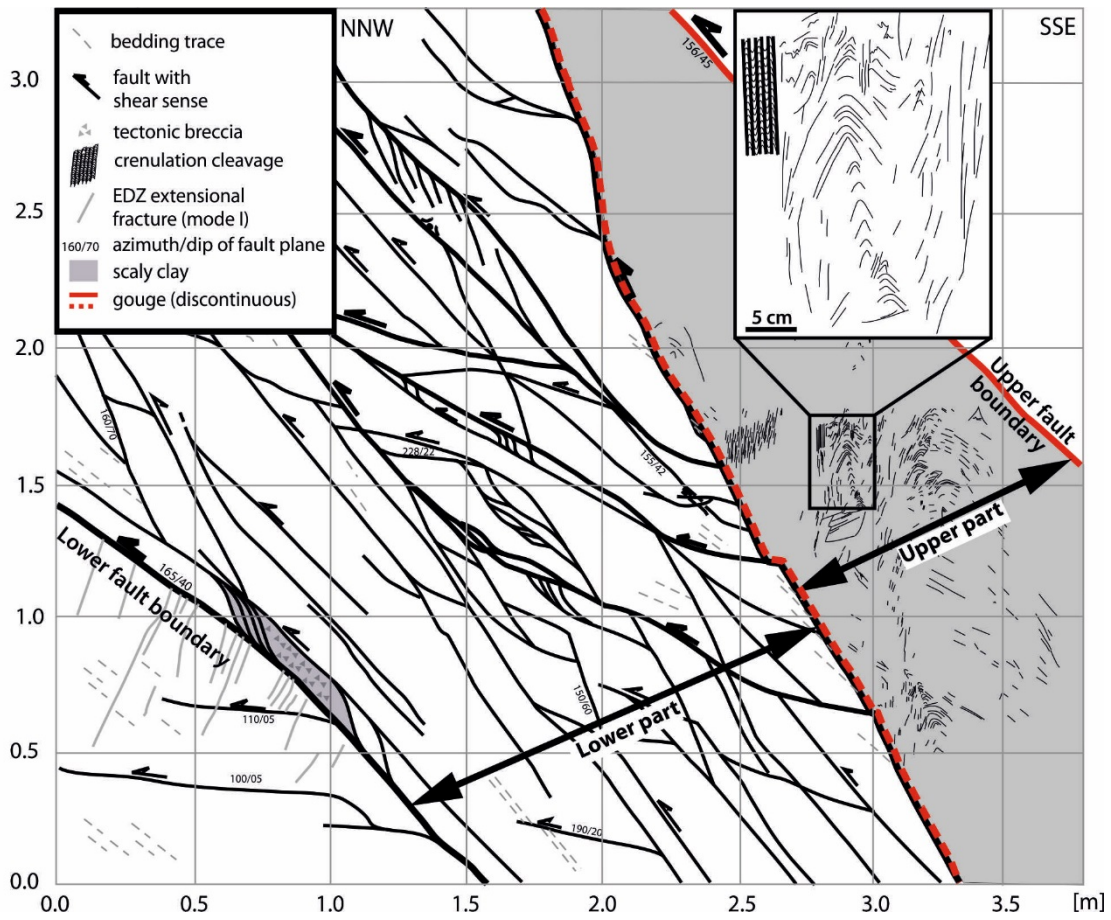
Figure 2: Small-scale map of the Main Fault in Gallery 08, viewing direction ENE, see Figure 1 for location (modified after Nussbaum et al. (2011)).

outcrop / drillcore mapping
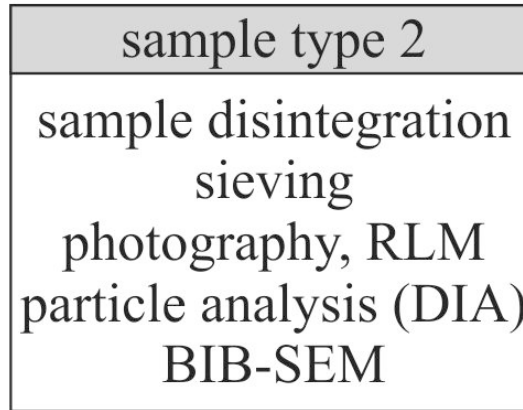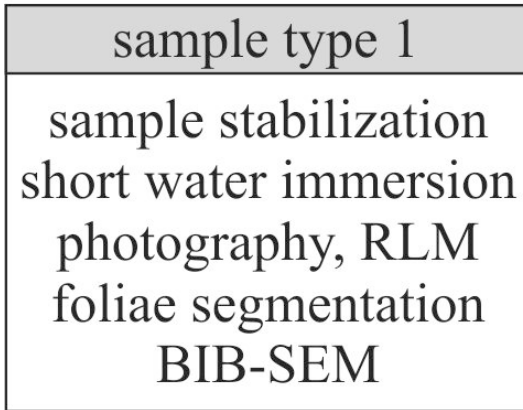sample selection
outcrop / drillcore sampling

sample type 1	sample type 2
sample stabilization short water immersion photography, RLM foliae segmentation BIB-SEM	sample disintegration sieving photography, RLM particle analysis (DIA) BIB-SEM

Figure 3: Sample types and corresponding workflow (RLM = reflected light microscopy, DIA = digital image analysis, BIB = broad-ion-beam, SEM = scanning electron microscopy).
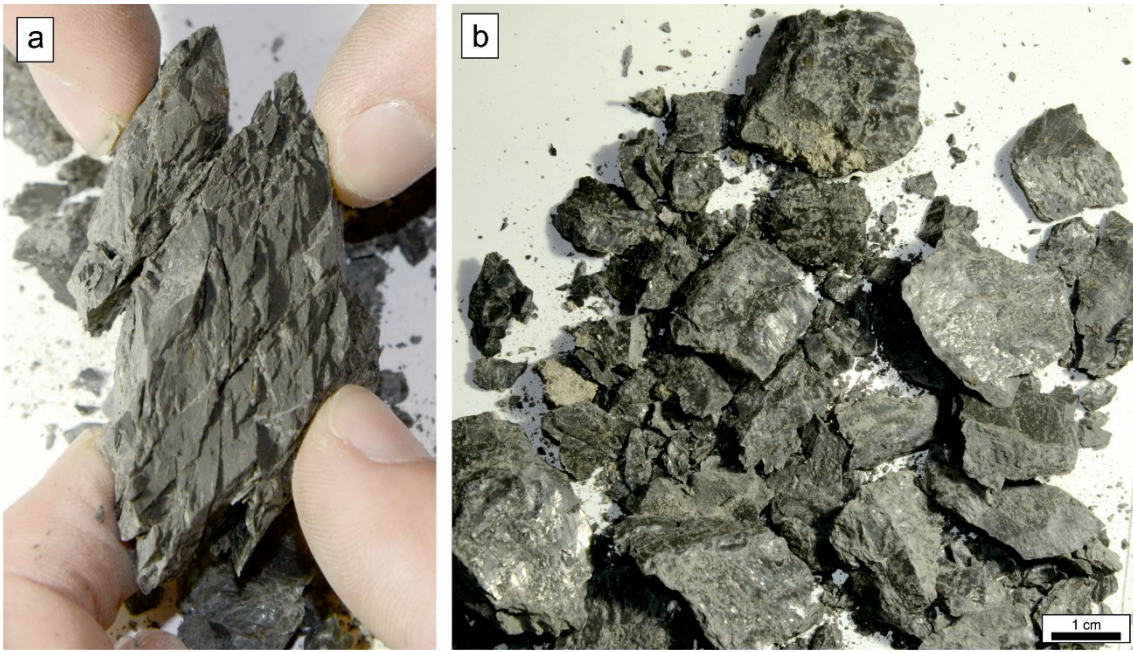
Figure 4: Scaly clay sample A5. A) intact, B) loose flakes (after gentle disintegration by hand).
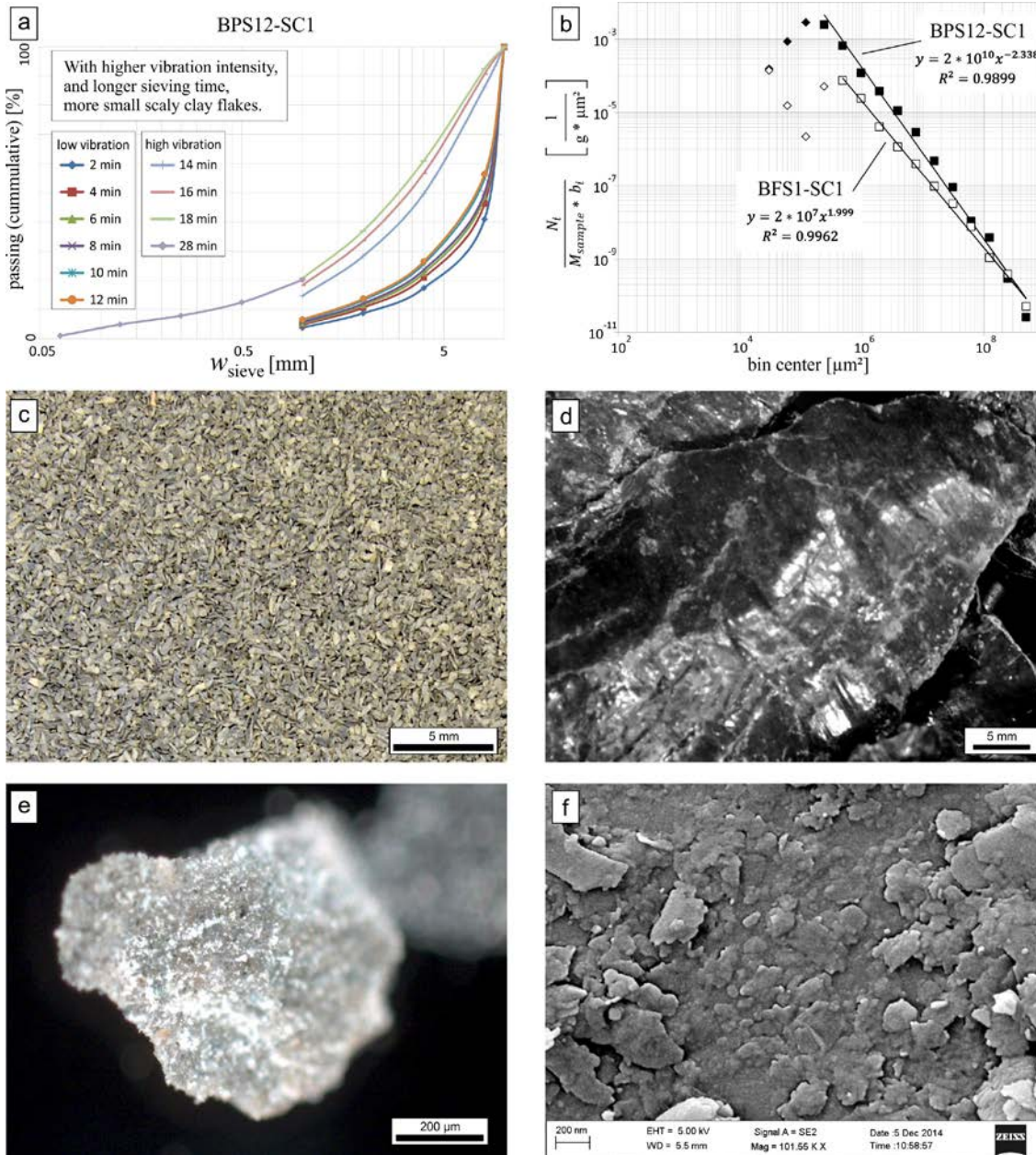
Figure 5: A) cumulative sieving curves of scaly clay microlithons from sample BPS12-SC1. B) log-log diagram illustrating the frequency of microlithon area sizes for the samples BPS12-SC1 and BFS1-SC1. The frequency (N_i) is noted corresponding to bin width (b_i) and normalized for sample mass (M_{sample}), the x-axis displays bin center. Diamonds are data points excluded in the regression analysis. See text for details. C) photograph of microlithons which passed the 0.25 mm but not the 0.125 mm sieve. Note the smooth, polished slickensided surface of the microlithons (D and E). F) shows the surface in high resolution SEM to be composed of elongated clay particles, which are only tens of nm-wide and oriented parallel to the surface. This structure is identical to slickensided surfaces presented in Laurich et al. (2014).
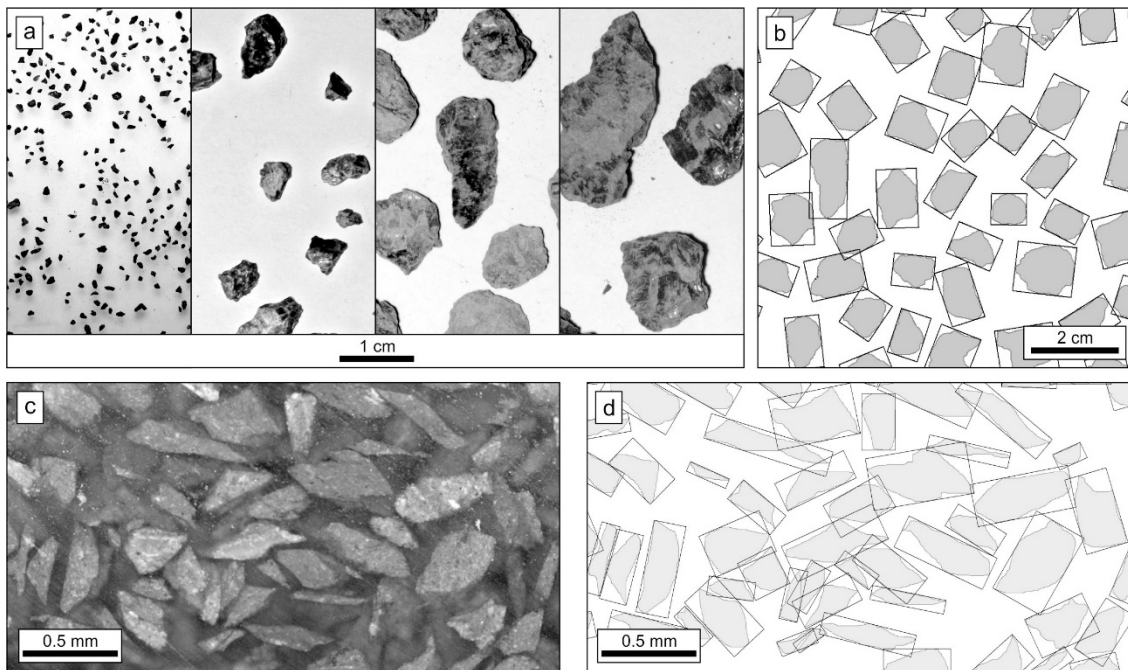
Figure 6: Disintegrated microlithons (A and C) and corresponding DIA segmentations with minimum bounding rectangles for shape description (B and D). A) photographs of dispersed microlithons of different sieve-fractions. C) is a reflected light micrograph showing resin-embedded microlithons from the 800 µm to 400 µm sieve-fraction. See text for details.

5
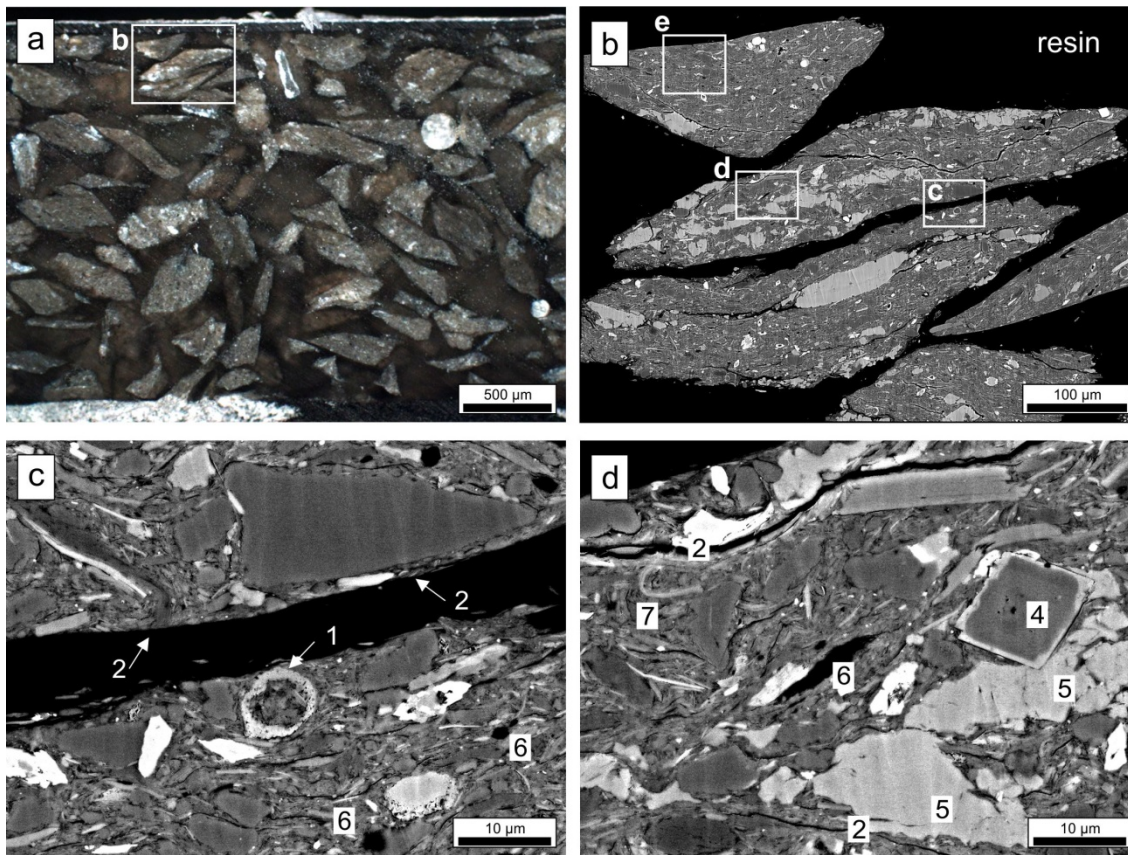
Figure 7: A) shows resin-embedded microlithons in RLM. B) – D) are BIB-SEM micrograph insets of A). B) shows fractured microlithons and calcite veins (bright). C) is a detail of B) showing a thin, microlithon bounding shear zone (2), an intact fossil (1) and unstrained OM (dark black, 6). D) is a detail of B) picturing microlithon internal shear zones (2), calcite overgrowth (4), calcite veins (5), strained OM (6) and bending of clay particles (bright mica, 7). Detail E) is shown in Figure 9b.
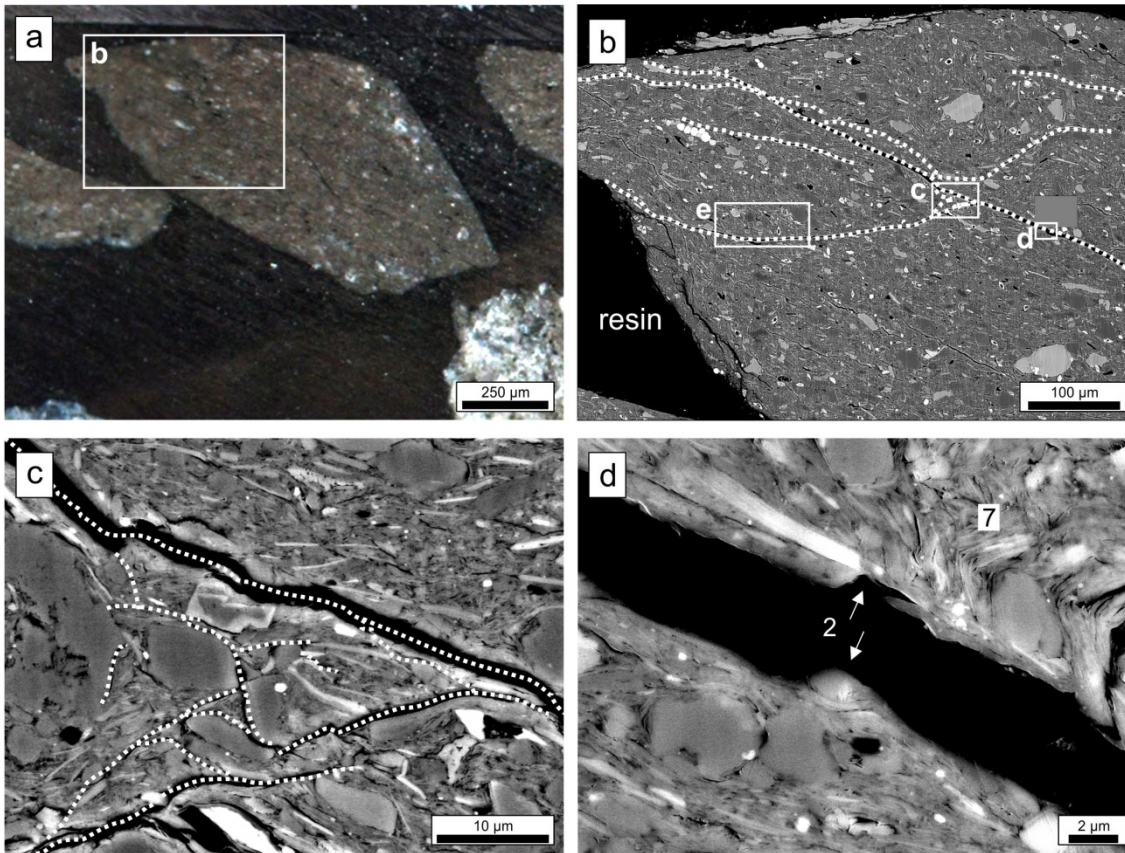
Figure 8: A) shows a resin-embedded microlithon in RLM. B) – D) are BIB-SEM micrograph insets of A). B) displays a microlithon with internal shear zones highlighted by dashed lines. C) is a detail of B showing a shear zone junction. D) is a detail of B showing a μm-thin, opened microlithon internal shear zone (2). We interpret the shear zone opening as a sampling artefact, with corresponding shapes of the fracture walls (arrows) and bend clay particles in the vicinity of the shear zone (7). Numbering as used in the following Figures. Inset E) is shown in Figure 9c.
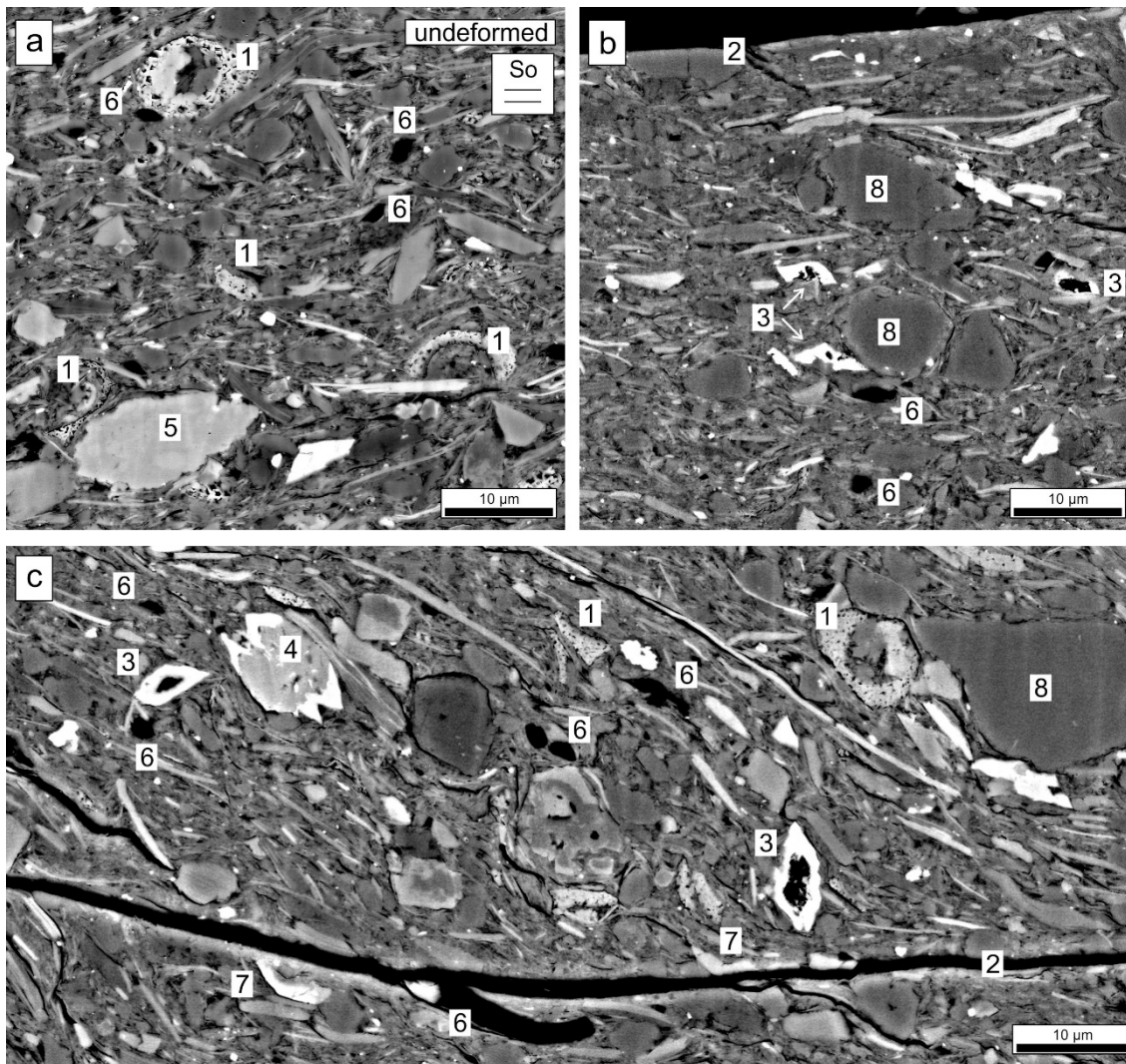
Figure 9: BIB-SEM micrographs comparing an undeformed fabric (A) and microlithon internal fabrics (B) and (C). A) derives from the sample shown in Figure 10a. The locations of B) and C) are given in Figure 7b and Figure 8b, respectively. The images show: intact to slightly strained fossils (1), µm-thin shear zones (2), pores in siderites (3), overgrowth (4), a calcite patch (5), dark OM (6), bend particles in the vicinity of a thin shear zone (7) and lobate SiO2 grains (8).
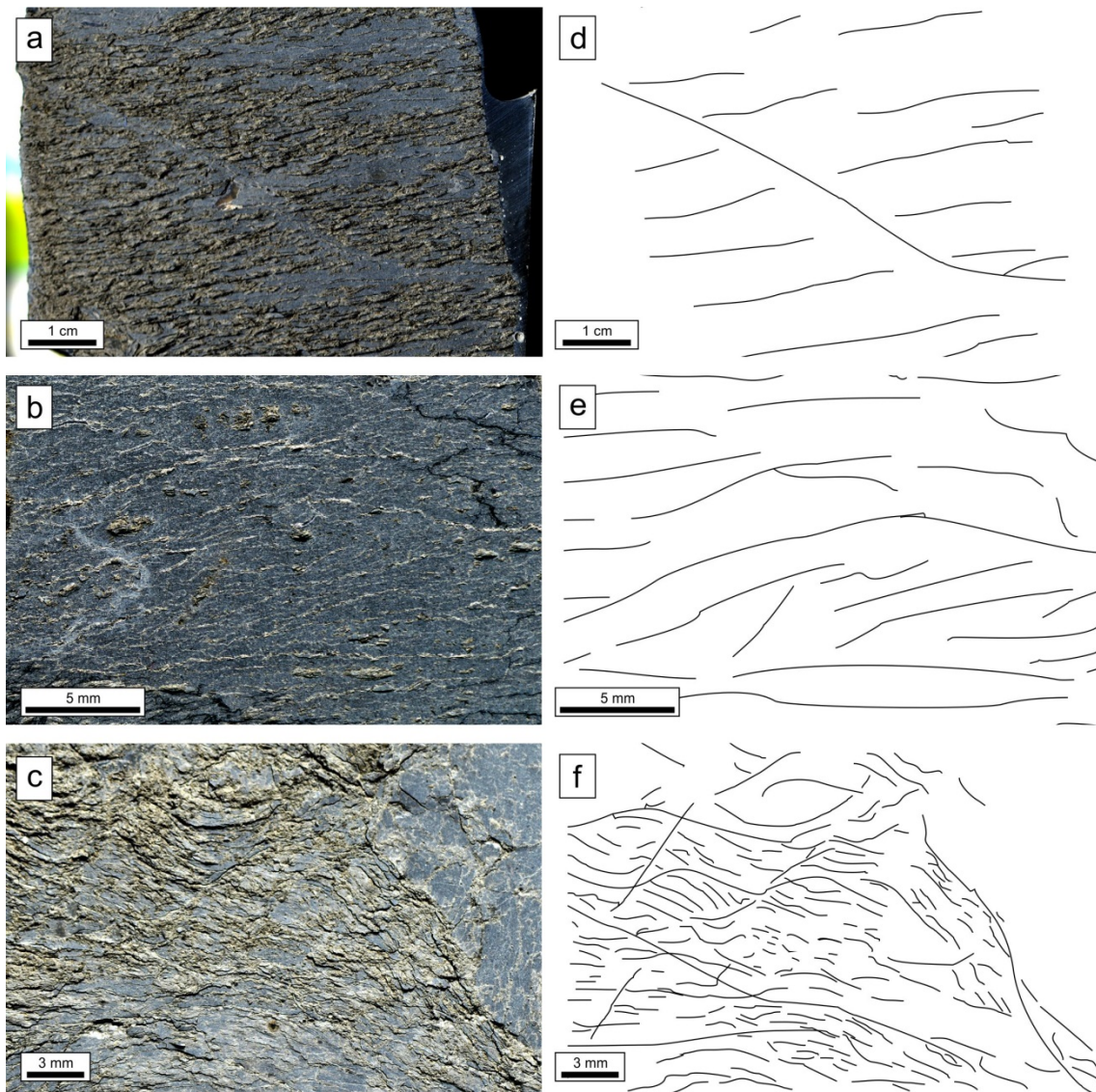
Figure 10: Photographs and sketches of water-immersed samples. A) sample V08 showing undeformed bedding foliation and one shear zone, B) sample V05 showing low strained scaly clay and (C) sample V14 being high strained scaly clay with higher density and complexity of shear zones. Right part in C) and F) likely resembles foliation perpendicular to viewing direction.

5

24
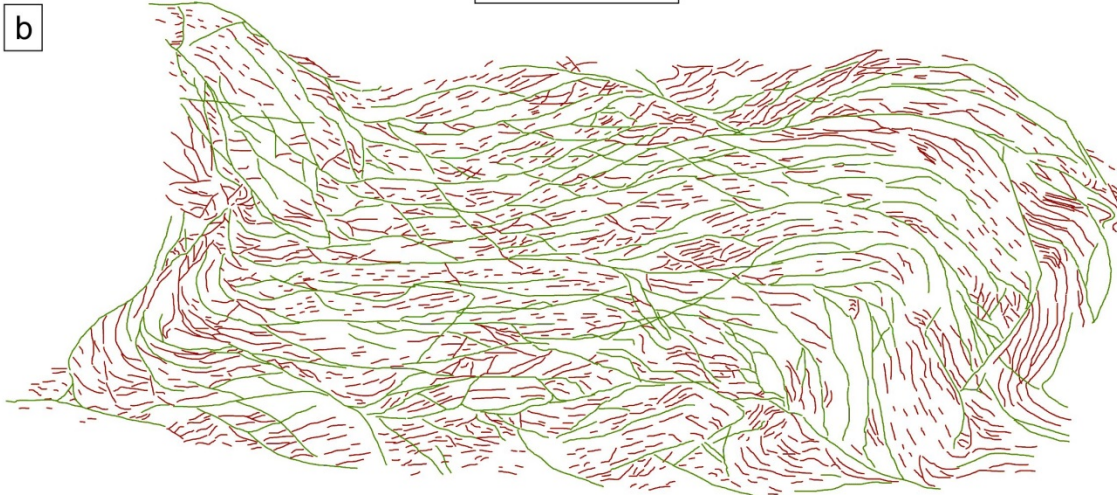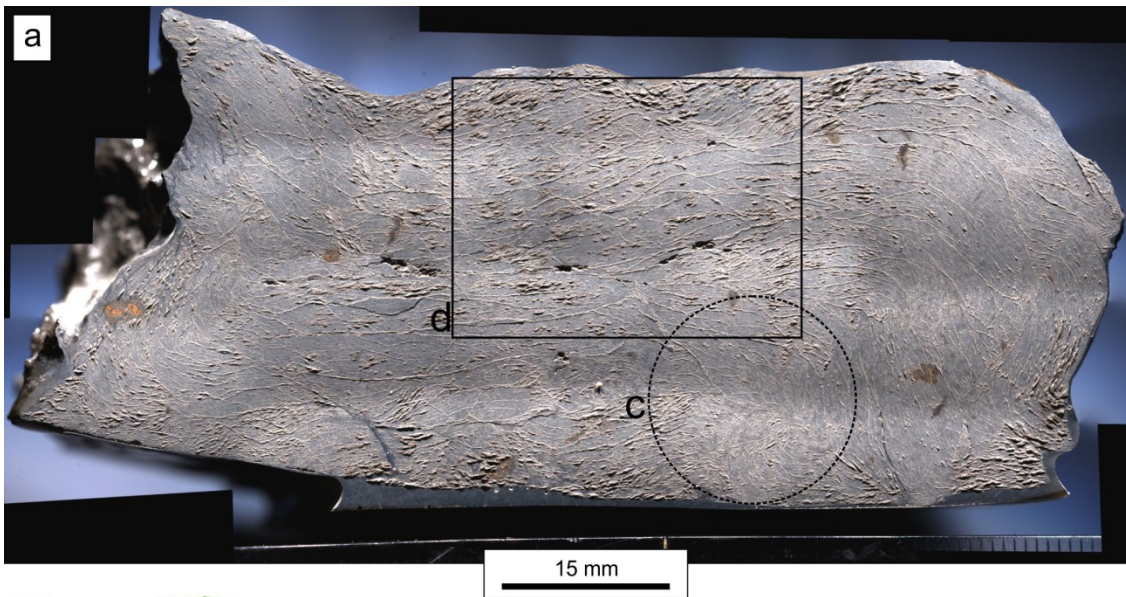
Figure 11: A) is a shaded light RLM-mosaic of a microfold in sample V12. B) shows foliation interpretations: thin shear zones (green) encasing lensoid microliths with sub-parallel bedding foliation (red). Note the overthrust-like structure in the microfold hinges in the left and right of the image. Circle c) is a detail shown in Figure 12. It derives from the counterpart half of the here shown sample. d) is shown in Figure 15.
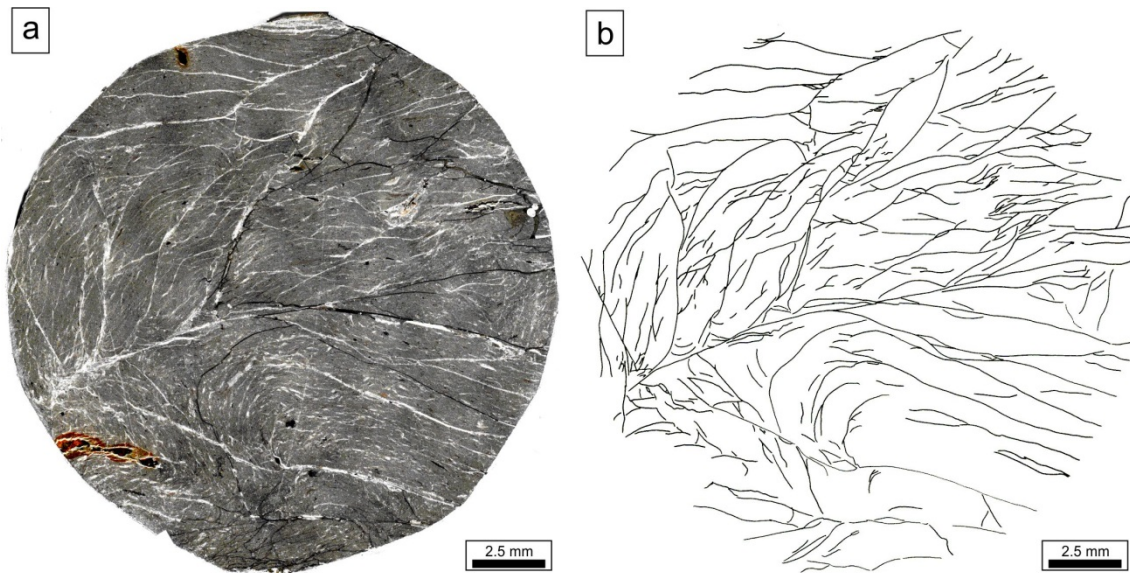
Figure 12: BIB-RLM micrograph and sketch of subsample V12-1 (see Figure 11 for location). Note the microfold in the lower sample part with bend foliation, while the microlithons in the upper part show a uniform foliation. There is no shear zone overprinting visible.

5
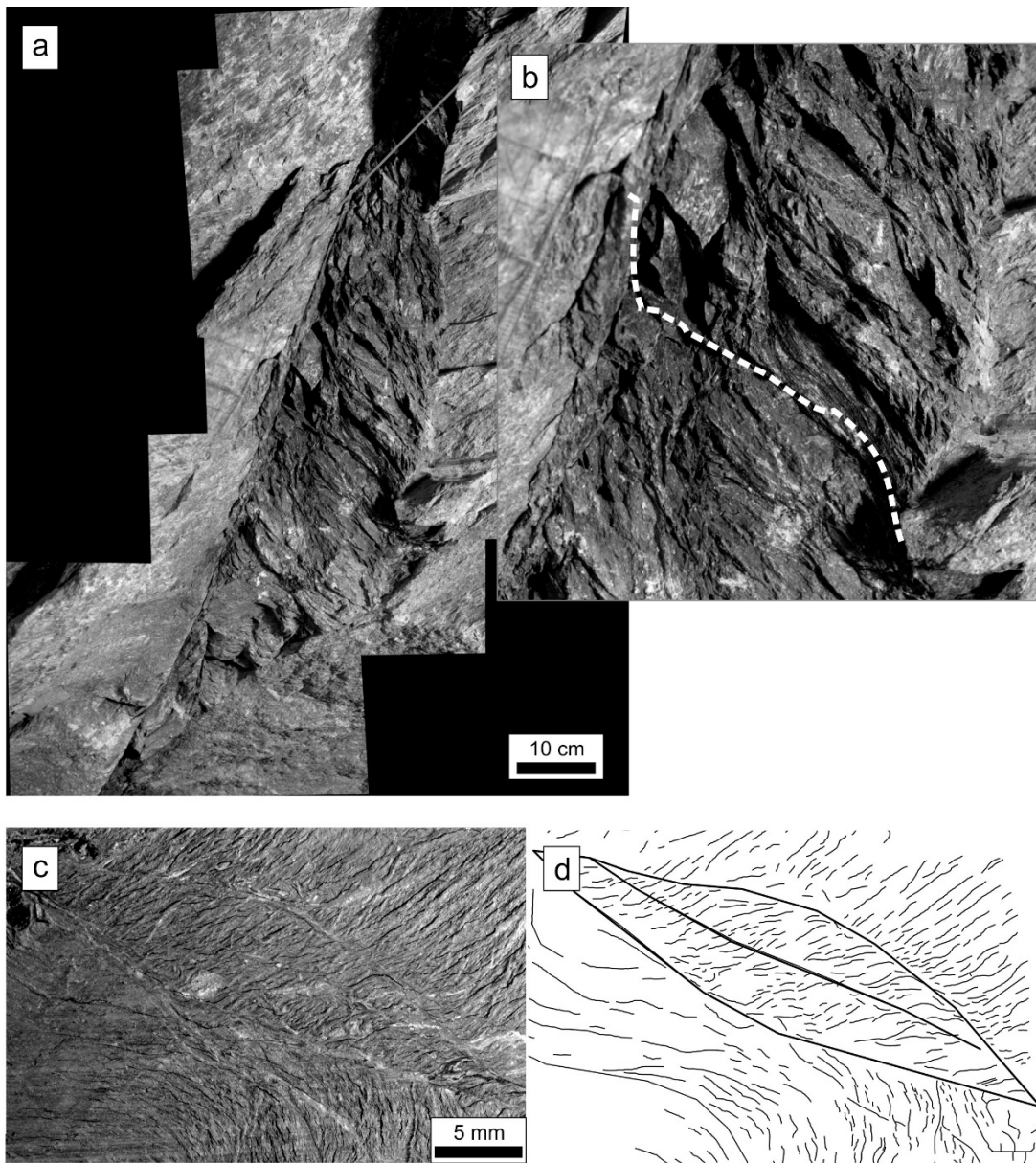
Figure 13: S-C foliations. A) and B) in outcrop-scale, viewing direction WSW at Gallery 98 (view Figure 1 for location). C) and D) in mm-scale in drill core sample BPS12-4 (location shown in Figure 14).
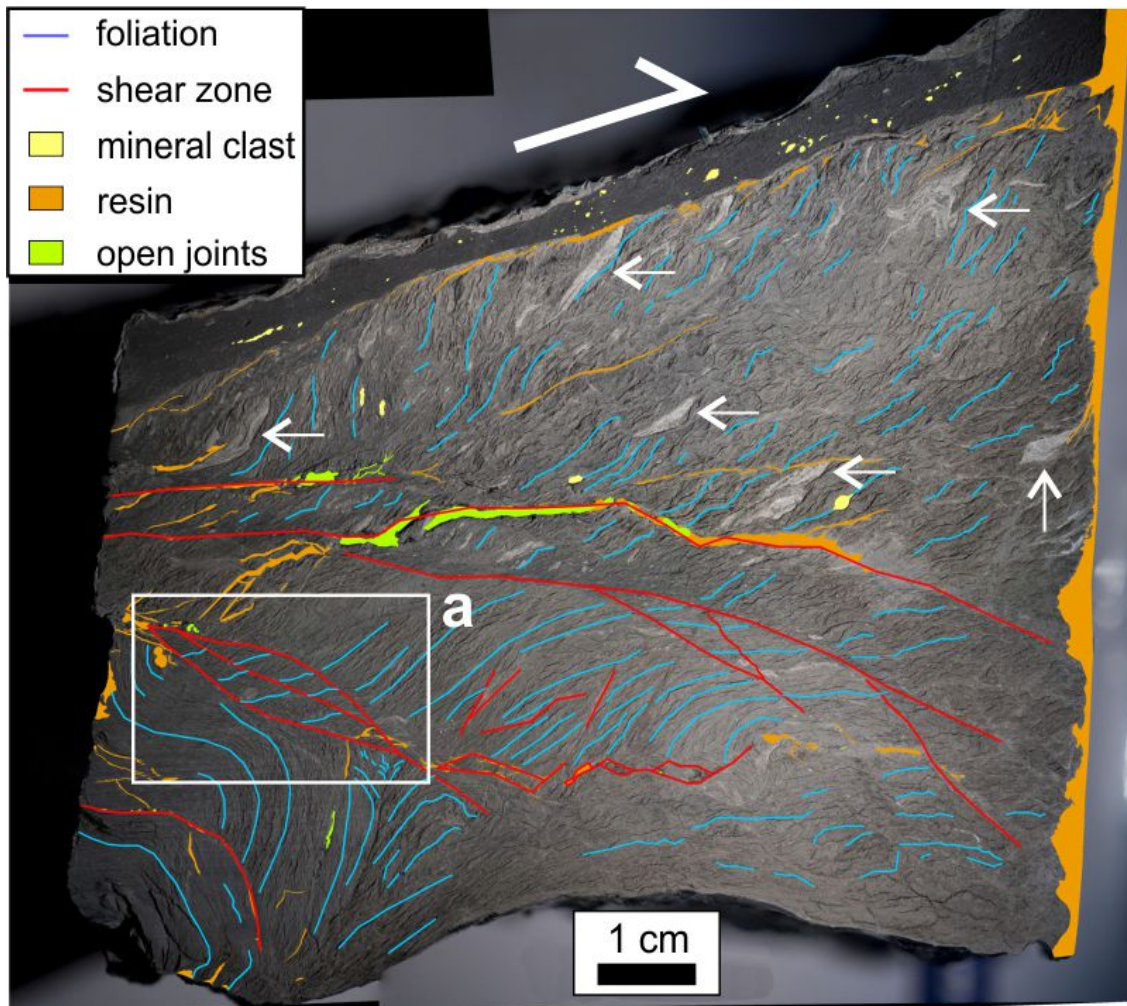
Figure 14: Shaded-light photograph and foliation sketches of water-immersed sample BPS12-4. Note the dark band of gouge on the sample top and brighter (calcite-rich) areas, indicated by arrows. a) is a detail shown in Figure 13c and d.
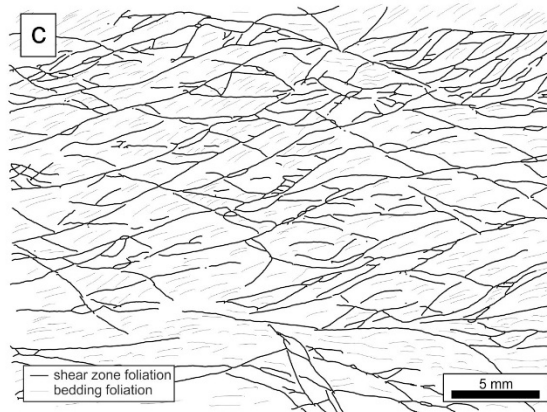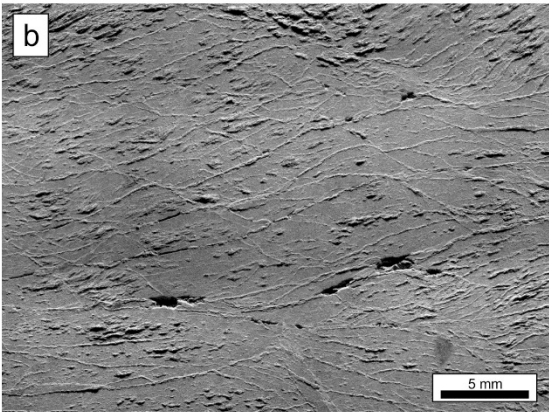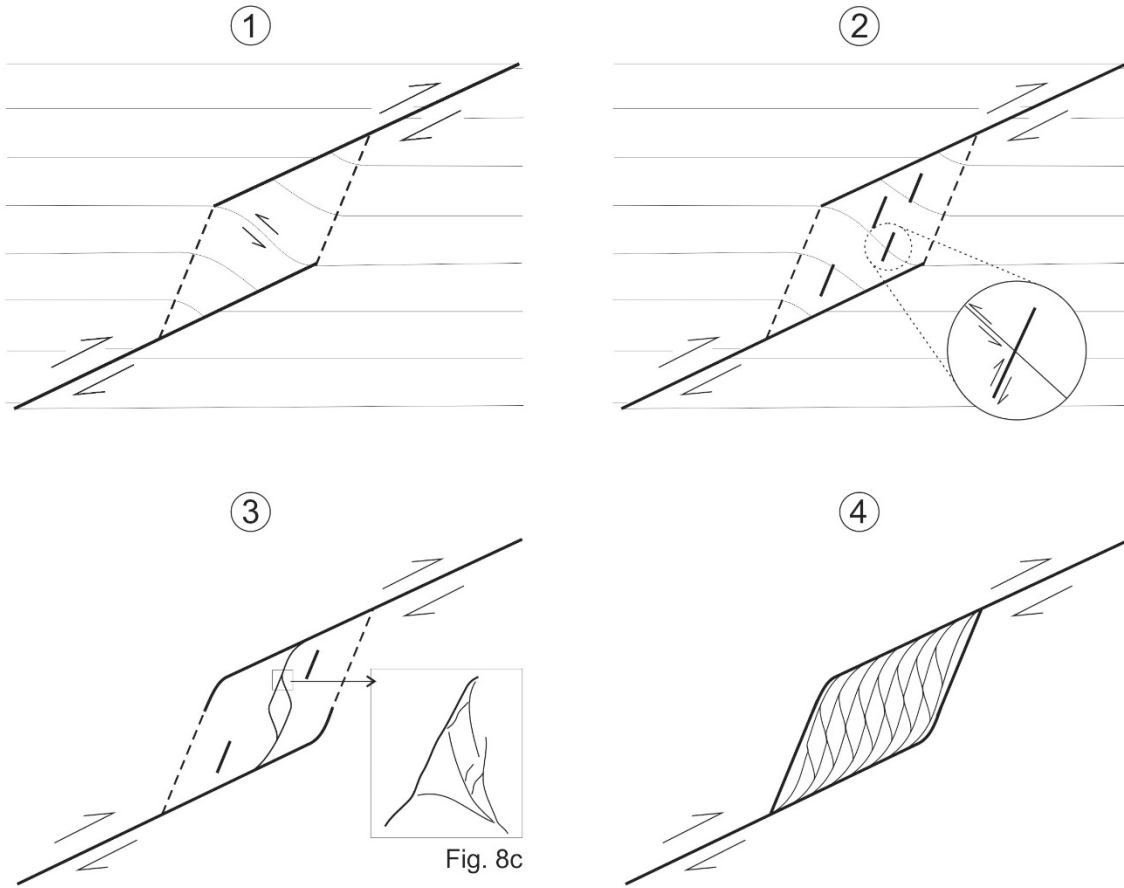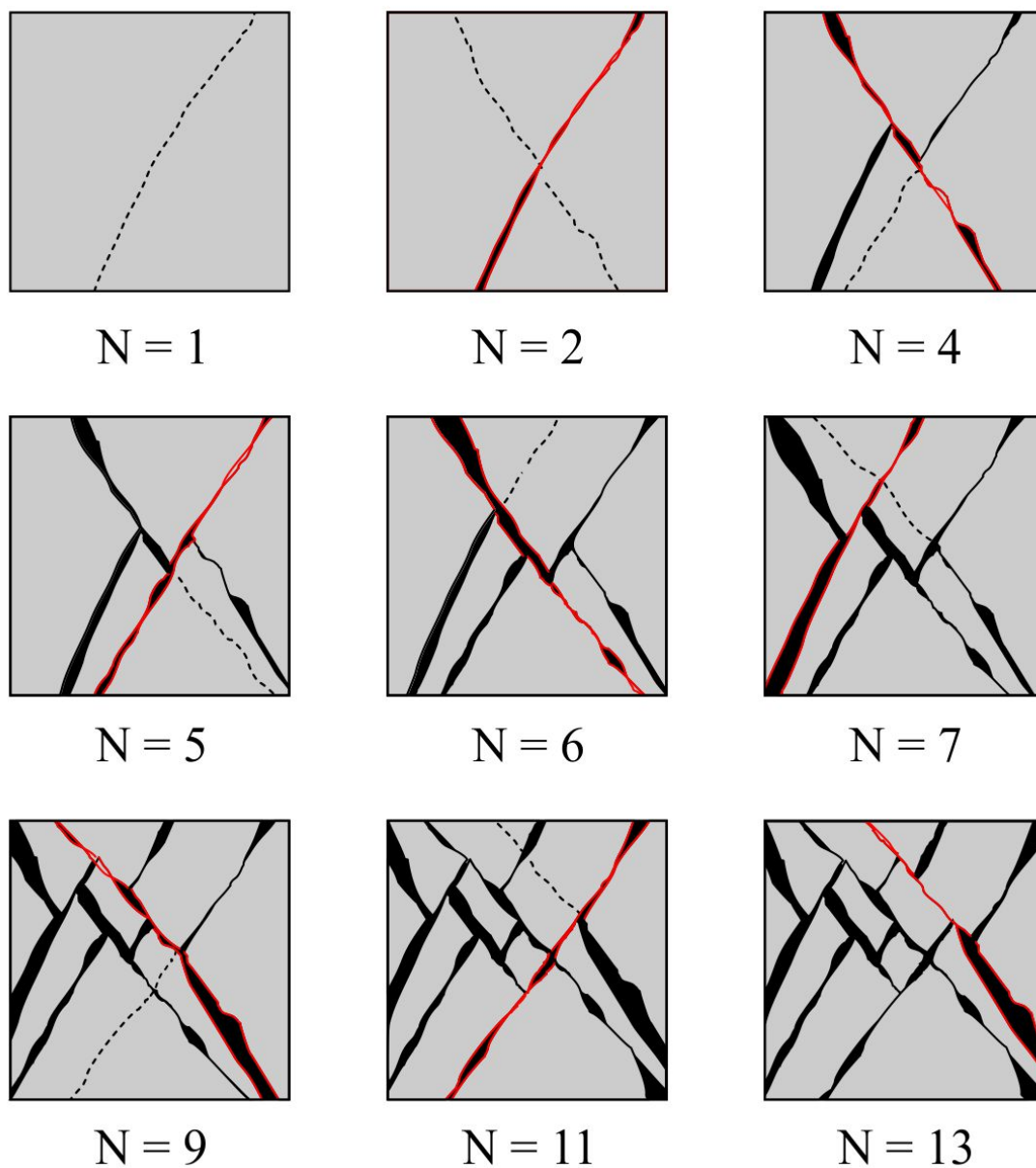
Figure 15: A) is a simplified mechanical model of the progressive development of anastomosing shear zones. (1): initial contractional relay (after Nicol et al., 2002) and relay internal development of a kink band by reorientation of bedding (compare to Figure 13). (2): development of relay-internal R-hears that themselves link as relays (3). The inset compares to shear zones shown

in Figure 8c. (4): Progressive development and linking of further shears. B) is an inset and C) a sketch from Figure 11. Note the similar shear zone pattern of (4) and (c).

Figure 16: Simplified mechanical model illustrating a rapidly increasing number of (smaller) microlithons by conjugate shearing. For better visibility, the model exaggerates the shear offset, which might lie in the range of only a few μm for scaly clay shear zones. Shear zone asperities create releasing and restraining bends, the first filled with calcite veins, the latter leading to geometrical 'locking-up', causing the development of new (smaller) microlithons.